

# Radio Spectrum and Distance of the SNR HB9

Denis A. Leahy<sup>1</sup> and Wenwu Tian<sup>1,2</sup>

<sup>1</sup> Department of Physics & Astronomy, University of Calgary, Calgary, Alberta T2N 1N4, Canada

<sup>2</sup> National Astronomical Observatories, CAS, Beijing 100012, China

Received xx, 2006; accepted xx, 2006

**Abstract.** New images are presented of the supernova remnant (SNR) HB9 based on 408 MHz and 1420 MHz continuum emission and H I-line emission data of the Canadian Galactic Plane Survey (CGPS) by the Dominion Radio Astrophysical Observatory (DRAO). Two methods of spectral index analysis for HB9 are presented and compared: one covers compact sources at both frequencies but is limited to the resolution of the 408 MHz image; the other covers compact sources only in the 1420 MHz image so is effective at higher spatial resolution. The second allows more detailed spectral index variation studies than the first. The two T-T plot methods and new integrated flux densities give spectral index ( $S_{\nu_2}/S_{\nu_1}$ ) for the whole of HB9 of 0.484, 0.032; 0.485; and 0.47, 0.06, respectively. These are lower than previous spectral index for HB9 ( $= 0.61$ ). Spatial variations of spectral index are derived using the second method and yield a lower spectral index for interior regions than for the rim. This can be explained by a standard curved interstellar electron energy spectrum combined with lower interior magnetic field compared to that near the outer shock, which results in a larger proportion of steep spectrum emission for lines-of-sight through the central body of the SNR. H I observations show structures probably associated with the SNR in the radial velocity range -5 to -8 km s<sup>-1</sup> and suggest a distance of 0.9–0.2 kpc for the SNR. This is consistent with the distance to the radio pulsar 0458+46, offset from the center of HB9 by 23°. However the pulsar spindown and kinematic ages are significantly greater than estimates of the SNR age: the Sedov age for HB9 is about 9 kyr and the evaporative cloud model yields ages of 4–10 kyr.

## 1. Introduction

The production of high-energy particles in our Galaxy is closely related to shock acceleration in supernova remnants (SNR). The study of the radio spectra produced by synchrotron emission by high-energy electrons in SNRs allows one to learn about the electron energy spectrum. HB 9 due to its large diameter is one of the best candidates for a study of SNR's spectral index spatial variations. Variations have been observed to occur in some other large angular sized SNRs (Leahy & Tian 2005; Tian & Leahy 2005, Uyaniker et al. 2004, Alvarez et al. 2001). The spectral index spatial variation of HB 9 has been noted by Leahy et al. (1998, 1991), but a new set of higher resolution and sensitivity observations of the Canadian Galactic Plane Survey (CGPS) combined with new spectral index analysis methods, impel us to carry out a new spectral index study of HB 9. A lack of direct estimates of the distance to HB 9 in previous research (Leahy & Roger 1991, Lozinskaya 1981, Milne 1979) is corrected here by an analysis of the new H I observations of HB 9.

## 2. Observations and Image Analysis

The continuum and H I emission data sets come from the CGPS, described in detail by Taylor et al. (2003). The data sets are mainly based on observations from the Synthesis Telescope (ST) of the Dominion Radio Astrophysical Observatory (DRAO). The spatial resolution of the continuum images of HB 9 is  $49^0 - 68^0$  at 1420 MHz and  $2.8^0 - 3.9^0$  at 408 MHz. The synthesized beam for the H I line images is  $58^0 - 80^0$  and the radial velocity resolution is 1.32 km/s. The DRAO ST observations are not sensitive to structures larger than an angular size scale of about  $3.3^0$  at 408 MHz and  $56^0$  at 1420 MHz. Thus the CGPS includes data from the 408 MHz all-sky survey of Haslam et al. (1982), sensitive to structure greater than  $51^0$ , and the Eelsberg 1.4 GHz Galactic plane survey of Reich et al. (1990, 1997), sensitive to structure greater than  $9.4^0$ . The large scale H I data is from the single-antenna survey of the CGPS area (Higgs & Tapping 2000) with resolution of  $36^0$ .

There are many compact sources (CS) overlapping HB 9's face. In order to better study the spectral index distribution of HB 9, we use and compare two methods to reduce the effects of compact sources on the SNR's spectral index. The first removes CS at both frequencies but is limited to the resolution of the 408 MHz image; the other removes CS only in the 1420 MHz image so is effective at higher spatial resolution. The first method was introduced by Tian and Leahy (2005) and the second was introduced by Leahy (2006). Both have been proved effective in removing CS contamination. We also analyze H I spectral line observations of HB 9 and estimate HB 9's distance here.

### 3. Results

#### 3.1. HB 9 Flux Densities at 408 MHz and 1420 MHz

The first row of Fig. 1 shows the CGPS 408 MHz (left) and 1420 MHz (right) images of HB 9 overlaid by boxes for spectral index determination. The 408 MHz and 1420 MHz CS-subtracted images are shown in the second row of Fig. 1. 160 CS at 1420 MHz and 61 CS at 408 MHz are detected within HB 9. The total flux densities of these CS are 12.0 Jy at 408 MHz and 5.6 Jy at 1420 MHz. After subtracting the flux of CS, the HB 9's flux density is 117.8 5.3 Jy at 408 MHz and 65.9 3.4 Jy at 1420 MHz. This gives a flux density-based 408–1420 MHz spectral index value of 0.47 0.06.

#### 3.2. HB 9 T-T Plot Spectral Indices

The principle of the T-T plot method is that spectral indices ( $T = T_0$ ) are calculated from a fit of a linear relation to the  $T_1 - T_2$  values of all pixels within a given map region.  $T_1$  is the brightness temperature of a map pixel at one frequency and  $T_2$  is for the second frequency. The higher resolution image has been smoothed to the lower resolution for the T-T plot comparison. The brightness temperature spectral index is derived from the slope of the line and the error from the uncertainty in slope of the line. The flux density spectral index is related to  $\alpha = +2$ . Spectral index refers to flux density spectral index in this paper.

The T-T plot method is first applied to the whole area covering HB 9 (the single big box of Fig. 1). Fig. 2 gives the 408–1420 MHz T-T plots for three cases (from left to right): case 1—maps including CS ( $\alpha_{\text{auto}} = 0.496 \pm 0.029$ ); case 2—CS subtracted from both 408 MHz and 1420 MHz maps ( $\alpha_{\text{auto}} = 0.484 \pm 0.032$ ); case 3—maps with Gaussian fits to CS subtracted from the 1420 MHz map only ( $\alpha_{\text{manual}} = 0.485$ ). The subscript *auto* refers to the case of an automated linear fit including all of the points, the subscript *manual* refers to the case of a manual fit done to the points excluding points due to CS. The points due to CS are clearly seen in the left plot of Fig. 2 if they have a significantly different slope than the points from the SNR. For the middle plot, CS are subtracted at both 408 and 1420 MHz. However, there are artifacts due to some CS subtracted at 1420 MHz but not 408 MHz and vice versa. Since the 408 MHz map is at lower spatial resolution the first case is much more common. For the right plot, since CS are subtracted only at 1420 MHz, points due to CS show up as vertical lines of points, with 408 MHz flux but no 1420 MHz flux. This occurs even if a CS has a spectral index similar to the diffuse SNR emission.

Generally, an erroneous value of spectral index is obtained using case 1 due to inclusion of CS. Case 2 can give a reliable spectral index if most CS are subtracted. However it often happens that the CS subtraction is quite imperfect due to the presence of the diffuse

SNR emission. This can be seen for 408 MHz by comparing the two left hand images in Figure 1: there are many fainter CS that cannot be reliably subtracted from the image, and in some cases where a CS is subtracted, an artifact is generated in the image by the imperfect subtraction process. These problems rarely occur in the higher resolution 1420 MHz image, as can be seen by comparing the two right hand images in Figure 1. For case 3, a manual fit to the points, ignoring the vertical lines due to CS, always gives a good result. For the particular case shown in Fig. 2, due to the large area of HB 9, the difference cases give similar results: for case 1 this is mainly just a coincidence due to the cancellation of errors due to CS with flatter and steeper spectra; for case 2 it is due to the dominance of SNR emission over errors in CS subtraction. However for smaller regions the difference in spectral index from the three methods can be large, so we use the case 3 analysis.

To study spatial variations in HB 9 we divide it into 52 regions (see the top plots of Fig. 1). The case 2 and 3 methods mentioned above both remove bright CS contamination. However the case 3 method also removes fainter CS detected at only 1420 MHz, so we use the case 3 method and give the results in Table 1 as manual. For comparison the spectral index from an automated fit including CS (case 1) is also given. Table 1 shows that case 1 and case 3 results can be quite different. Fig. 3 shows T-T plots for region 21: for case 1 (left,  $\text{auto} = 0.51 \pm 0.01$ ), case 2 (middle,  $\text{auto} = 0.88 \pm 0.11$ ), and case 3 (right,  $\text{manual} = 0.61$ ). The spectral index for case 1 (CS included) is dominated by the single bright CS. Case 2 (CS subtracted at 408 MHz and 1420 MHz) gives an erroneous (too large) value of spectral index. The reason is that the Gaussian fitting, in the presence of the diffuse emission, to the strongest CS gave too small a 408 MHz flux, resulting in a residual 408 MHz flux in the 408 MHz CS subtracted map. The advantage of case 3 (subtracting CS at only 1420 MHz) is more apparent here, since there is not overcrowding of the CS in the T-T plot, like there was in Fig. 2 (right). This allows easy identification of the CS, including the faint CS at  $\text{TB}(1420) = 5.8\text{K}$ , and fitting to the remaining points.

A histogram of the T-T plot spectral index values from Table 1 is shown in Fig. 4. The dashed line shows the spectral indices obtained from automatic fits, including CS at both 408 MHz and 1420 MHz (case 1); the solid line shows the spectral indices obtained from manual fits for CS subtracted at 1420 MHz (case 3). The effect of CS on the spectral index distribution is clear: there is a second peak in the histogram introduced at 0.7 to 0.9 due to CS, whereas the SNR only emission (case 3) has a distribution of indices between 0.4 and 0.8.

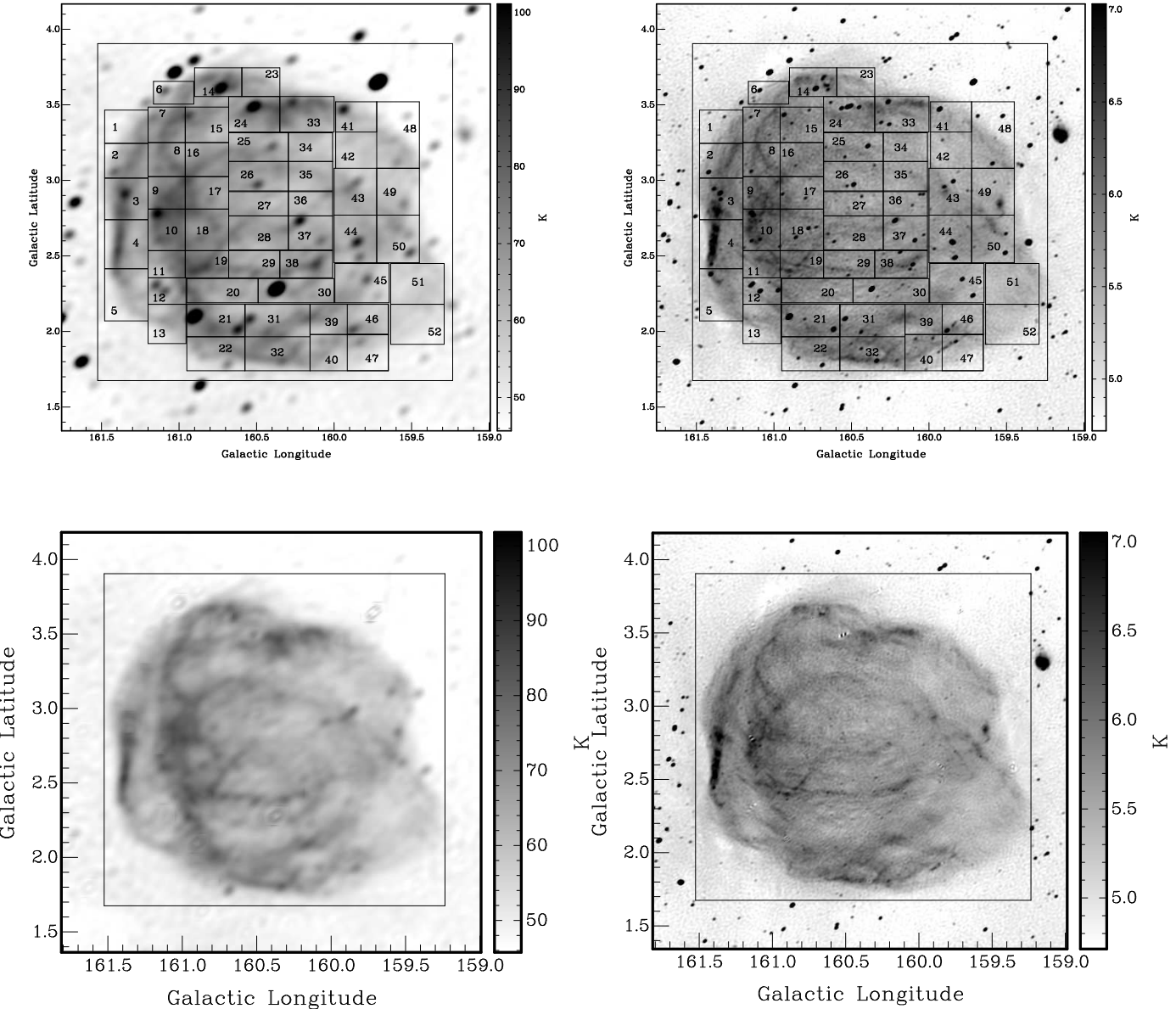


Fig. 1. The first row shows the images of HB 9 at 408 MHz (left) and 1420 MHz (right).

The second row shows the 408 MHz image with compact sources (CS) subtracted (left) and the 1420 MHz image with CS subtracted (right). The single large box is the area used for T-T plots of the whole of HB 9; the 52 small boxes labeled with numbers show areas used for T-T plots of subareas of HB 9.

### 3.3. H I Emission

We have searched the CGPS H I images at different radial velocities for features in the H I which might relate to the morphology of HB 9. There is emission which is spatially associated with the boundary of HB 9 in the velocity range -22 to -25 km/s, but not at other velocities. This indicates that this H I is very likely physically associated with the

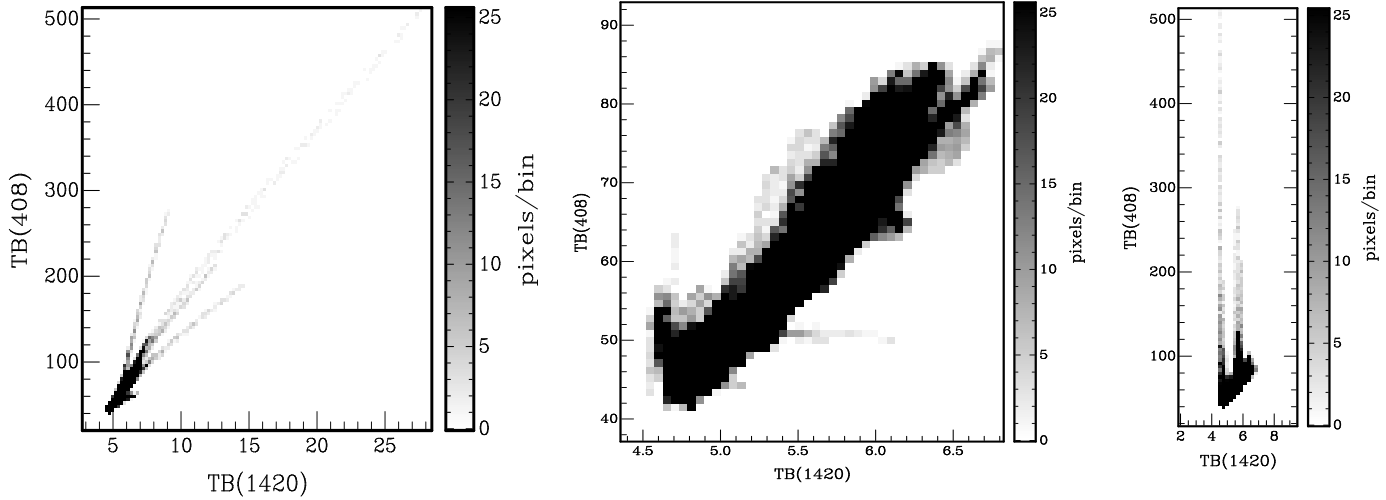


Fig. 2. 408 MHz-1420 MHz T-T plots for the whole of HB 9: including CS (left,  $m_{auto} = 0.496 \pm 0.029$ ); for CS subtracted from both 408 MHz and 1420 MHz maps (middle,  $m_{auto} = 0.484 \pm 0.032$ ); for CS subtracted from 1420 MHz map only (right,  $m_{manual} = 0.485$ ).

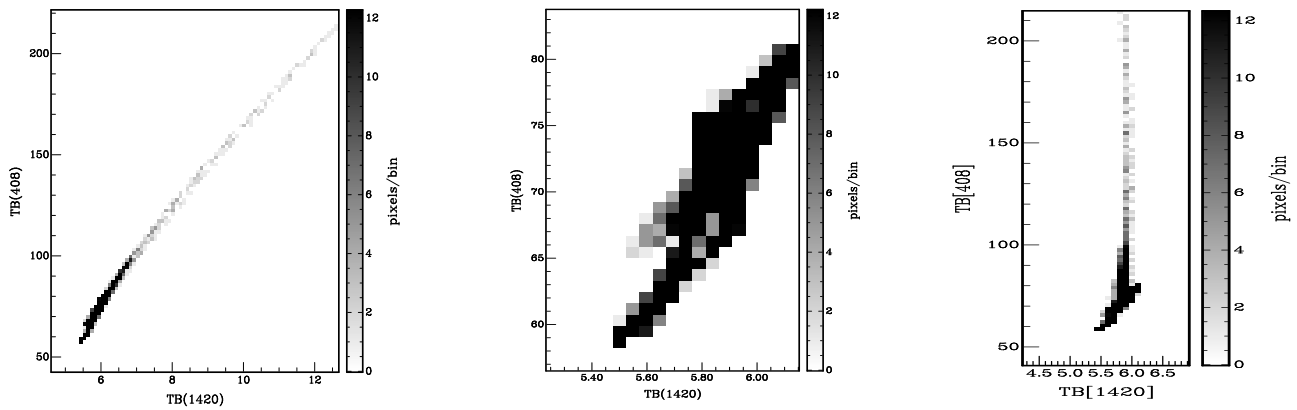


Fig. 3. 408 MHz-1420 MHz T-T plots of region 21: including CS (left); for CS subtracted from both 408 MHz and 1420 MHz maps (middle); for CS subtracted from 1420 MHz map only (right).

SNR. Fig. 5 shows maps of the H I emission in the 4 channels in -22 to -25 km/s, with a contour of continuum emission at 1420 MHz to show the edge HB 9.

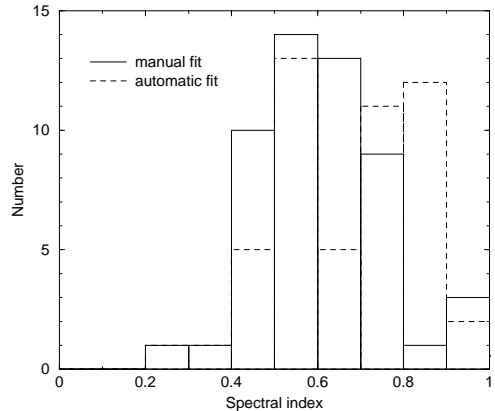


Fig. 4. Histogram of spectral indices in HB 9.

Fig. 5. H I emission in the field centered on HB 9 from  $-5$  to  $-8$  km/s, with 1420 MHz continuum contour at  $5.3$  K  $T_B$  indicating HB 9. The radial velocity of each map is indicated at top left.

Table 1. HB 9 408–1420 MHz Spectral Index for Regions 1 to 52

Region	case1	case3	Region	case1	case3
1	0.58	0.01	27	0.75	0.07
2	0.51	0.01	28	0.85	0.11
3	0.55	0.02	29	1.05	0.08
4	0.50	0.01	30	1.38	0.01
5	0.44	0.04	31	0.75	0.02
6	0.65	0.09	32	0.52	0.02
7	0.85	0.09	33	0.82	0.03
8	0.87	0.09	34	0.87	0.11
9	0.86	0.03	35	0.81	0.11
10	0.72	0.10	36	0.77	0.02
11	0.78	0.05	37	0.77	0.03
12	0.52	0.05	38	0.81	0.02
13	0.57	0.04	39	0.83	0.04
14	0.69	0.02	40	0.29	0.05
15	0.91	0.03	41	0.42	0.02
16	0.93	0.03	42	0.55	0.23
17	0.75	0.02	43	0.77	0.03
18	0.77	0.10	44	0.56	0.04
19	0.88	0.07	45	0.52	0.02
20	0.85	0.07	46	0.53	0.02
21	0.51	0.01	47	0.35	0.02
22	0.50	0.02	48	0.51	0.02
23	0.72	0.02	49	0.57	0.03
24	0.84	0.02	50	0.76	0.03
25	0.70	0.09	51	0.45	0.03
26	0.69	0.05	52	0.70	0.14
					0.50

#### 4. Discussion

##### 4.1. Distance of HB 9, age, and possible association with pulsar 0458+46

For the velocity range of -5 to -8 km/s, using circular galactic rotation velocity  $V_R = V_0 = 220$  km/s,  $R_0 = 8.5$  kpc, yields distance to HB 9 of  $d = 0.9$ –0.2 kpc. This distance agrees well with previous estimates: greater than 1 kpc derived from measurements of radial velocity of H I lamellae by Lozinskaya (1981); about 1.1 kpc from the X-ray properties of HB 9 by Leahy (1987); and 1.3–1.8 kpc from surface-brightness-diameter relations by Milne (1979) and Caswell & Lerche (1979).

Since the angular size of HB 9 is  $130^0$  by  $120^0$ , the mean radius is 18 pc at 1.1 kpc.

A Sedov model (Cox D., 1972) can be applied, using the X-ray temperature and X-

ray ux from Leahy and A schenbach (1995). To get a radius of 20pc, one obtains an age of about 9 kyr and explosion energy  $E_{51}$  (in  $10^{51}$ erg) divided by initial density  $n_0$  ( $\text{in cm}^{-3}$ ) of  $E_{51}/n_0 = 10$ . The Sedov model likely does not apply to HB 9 as noted by Leahy and A schenbach (1995), based on the X-ray morphology and uniform observed X-ray temperature: the White and Long (1991) evaporative cooling model better explains these features. The White and Long model is applied to HB 9 at distance of 1.1 kpc for the range of parameters which give a nearly uniform temperature profile at 0.8 keV and an appropriately centrally brightened X-ray profile ( $\gamma = 10$  and  $C = 20$  to  $C = 50$ ). The resulting preshock intercloud density is  $2\text{--}15 \cdot 10^{-3} \text{cm}^{-3}$ , the age is 4–10 kyr and the explosion energy is  $0.1\text{--}0.5 \cdot 10^{51}$ erg.

The radio pulsar 0458+46 is only  $23^0$  from the center of HB 9. It has a DM distance 1.8 kpc, spin-down age  $1.8 \times 10^6$  yr and transverse velocity 95.5 km/s (Manchester et al., 2005). The DM distance is expected to be larger than its true distance, from the HI data, due to the extra DM introduced by the extra electron density in the SNR shell. The spin-down age assumes a fast initial spin so is an overestimate of true age. The pulsar's kinematic age based on its transverse velocity is  $7 \times 10^4$  yr, several times larger than HB 9's age from either Sedov or evaporative cloud models. Thus an association between the pulsar and HB 9 is possible, but only if it was a somewhat off-center explosion: the kinematic age is reduced to 10,000 yr if the explosion center is  $3^0$  from the current pulsar position. Better X-ray observations of HB 9 should determine the nature of SNR, and give an improved SNR age value.

## 4.2. HB9 Spectral Index

Leahy & Roger (1991) gave a mean T-T plot spectral index of 0.61 for HB 9. Our T-T plot spectral index from the whole of HB 9 ( $= 0.484 \pm 0.032$ ) is much smaller, but consistent with the integrated flux density-based spectral index ( $= 0.47 \pm 0.06$ ). Two main factors should be responsible for this. First, there is a significant change (3-4 K difference) in SNR brightness temperature at 1420 MHz compared to earlier data sets (e.g. Leahy & Roger, 1991), and no such change in the 408 MHz images. Second, the present observations have higher resolution and sensitivity, so more compact sources have been resolved and subtracted in the images of HB 9.

Now we discuss the spectral index variations with location within HB 9. Since the integrated  $ux$  and  $T-T$  plot spectral indices for the whole of HB 9 agree each other, the laminetary emission (measured by the  $T-T$  plot method) and the total emission (laminetary plus spatially smooth emission) have the same spectral index. When one looks at `spectralindex` (`case3` in Table 1) vs. position, one finds that the flatter spectral indices ( $< 0.5$ ) are all associated with the SNR limb and that all of the steeper values ( $> 0.7$ ) are associated with the interior. The mean and standard deviation of spectral

indices for all limb regions are 0.49 and 0.11, whereas the values for the interior regions are 0.67 and 0.12.

A general discussion of mechanisms for changing spectral index is given in Leahy & Roger (1998). Absorption processes and electron energy losses from ionization act more effectively at lower frequencies and result in spectral flattening. Synchrotron and inverse-Compton act at high energies and steepen the spectrum. If the electron energy spectrum is curved then spatial variations in spectral index can occur due to variations in magnetic field, which determines the observed synchrotron frequency for a given electron energy. The diffuse galactic electron spectrum, has an electron energy index steepening from 2.0 below 2 GeV to 2.6 above 5 GeV, then to 3.5 above 40 GeV, corresponding to synchrotron index increasing from = 0.5 at low frequency to = 1.25 at high frequency. For a fixed observing frequency, increasing magnetic field,  $B$ , means sampling lower electron energies, so that spectral index flattens with increasing  $B$ .

For HB 9, the steeper index for interior regions, for which the line of sight goes through the whole SNR, could be interpreted as due to lower  $B$  for the interior compared to the rim; stronger synchrotron losses for the interior; or stronger absorption effects at the rim. For the Cygnus Loop (Leahy & Roger, 1998) low frequency observations confirm that the NE rim shows the effects of thermal plasma absorption. However for HB 9, previous studies have not found significant weakening of the radio brightness at the rim at low frequencies. This leaves the first two causes to examine more closely. The radio morphology of HB 9 is consistent with a low brightness interior surrounded by a brighter shell with filaments: the image at 1420 MHz in Figure 1 shows this most clearly. The highest compression in an SNR should occur just inside the forward shock, where the optical filaments form. Thus one expects the highest magnetic fields and highest synchrotron emissivity in the high compression regions. This now explains the observed spectral index variations: larger magnetic field at larger radius within the SNR gives flatter radio spectrum from larger radius. Thus lines-of-sight through the interior have more steep spectrum (from low magnetic field regions) fixed in with the afteremission from larger radius.

We compare with previous work on spectral index variations in HB 9. Leahy & Roger (1991) reported spectral index variations, but as noted above the old 1420 MHz image has a lower brightness temperature scale, as well as lower resolution and sensitivity. That study only removed the brightest compact sources, unlike the current study using the new analysis method. The study of Leahy et al. (1998) used the old DRAO 408 MHz and 1420 MHz observations and combined those with existing 2695 MHz and 4850 MHz data from the Eddington telescope, observations at 151 MHz with the Cambridge Low-Frequency synthesis telescope and new 232 MHz observations with the Beijing Astronomical Observatory Miyun telescope. The published maps of spectral index using 151 or 232 MHz suffered from lack of low-order spacings, and the mean derived

spectral indices for 151–232 MHz and 232–408 MHz indicate that the brightness scale for 232 MHz map was too large. The spectral index maps for the different frequency pairs are quite different indicating that brightness temperature scale errors, including that known for the old 1420 MHz map, and other errors in the data, as well as incomplete compact source rem oval, dominate the derived spectral indices over true SNR variations. However, it is interesting to note that the frequency-averaged spectral index map, which should suffer least from these errors, bears some similarity to the results presented here: steeper index from the central regions than the rim.

## 5. Conclusion

We present new higher sensitivity and higher resolution images of the SNR HB 9 at 408 MHz and 1420 MHz, and study its radio spectrum, corrected for point source flux densities using new improved methods. The T-T plot spectral index for HB 9 agrees with the integrated flux-density based 408–1420 MHz spectral index. A study of spatial variations reveals lower spectral index for interior regions than for rim regions. This can be explained by a standard curved interstellar electron energy spectrum combined with variable magnetic field. Due to lower compression, a lower magnetic field in the interior, compared to that near the outer shock, results in steeper spectrum emission from the interior. Thus a larger proportion of steep spectrum emission for lines-of-sight through the central body of the SNR results in an observed steeper spectral index for interior regions. Based on H I features associated with HB 9, we obtain a distance of 1.1 kpc, and give updated Sedov and evaporating cloud model parameters for the SNR. We discuss the possible association between the pulsar and HB 9, and conclude that more evidences are necessary to support this possible association.

Acknowledgments. We acknowledge support from the Natural Sciences and Engineering Research Council of Canada. The DRAO is operated as a national facility by the National Research Council of Canada. The Canadian Galactic Plane Survey is a Canadian project with international partners.

## References

- Alvarez, H., Aparici, J. & Reich, P., 2001, *A & A*, 372, 636
- Caswell, J. L., Lerche, I., 1979, *MNRAS*, 187, 201
- Furst, E., Reich, W., Reich, P. and Reif, K., 1990, *A & AS*, 85, 691
- Haslam, C. G. T., Salter, C. J., Stöbel, H. and Wilson, W. W., 1982, *A & AS*, 47, 1
- Higgs, L. A. and Tapping, K. F., 2000, *AJ*, 120, 2471
- Leahy, D. A., 2006, *ApJ*, accepted
- Leahy, D. A., Zhang, X. Z., Wu, X. J. and Lin, J. L., 1998, *A & A*, 339, 601
- Leahy, D. A., Aschenbach, B., 1995, *A & A*, 293, 853
- Leahy, D. A. & Roger, R. S., 1991, *ApJ*, 101, 1033

Leahy, D. A. & Roger, R. S., 1998, *ApJ*, 505, 784

Leahy, D. A., 1987, *ApJ*, 322, 917

Manchester, R. N., Hobbs, G. B., Teoh, A. & Hobbs, M., 2005, *AJ*, 129, 1993

Milne, D. K., 1979, *AuJPh*, 32, 83

Reich, W., Reich, P. and Furst, E., 1990, *A&AS*, 83, 539

Reich, W., Reich, P. and Furst, E., 1997, *A&AS*, 126, 413

Engelink, R. B., Tang, Y., de Bruyn, A. G., et al., 1997, *A&AS*, 124, 259

Routledge, D., Dwek, P. E., Landecker, T. L. et al. 1991, *A&A*, 247, 529

Taylor, A. R., Gibson, S. J., Peracaula, M. et al., 2003, *AJ*, 125, 3145

Tian, W. W. & Leahy, D. A., 2005, *A&A*, 436, 187

Lozinskaya, T. A., 1981, *SvAL*, 7, 17

Uyaniker, B., Reich, W., Yar, A. & Furst, E., 2004, *A&A*, 426, 909

White, R., Long, K., 1991, *ApJ*, 373, 543